RAA 2019 Vol. **19** No. **5**, 74(10pp) doi: 10.1088/1674–4527/19/5/74

http://www.raa-journal.org *http://iopscience.iop.org/raa*

Research in Astronomy and Astrophysics

Measurements of atmospheric turbulence parameters at Vainu Bappu Observatory using short-exposure CCD images

Sreekanth Reddy V., Ravinder Kumar Banyal, Sridharan R. and Aishwarya Selvaraj

Indian Institute of Astrophysics, Bangalore 560034, India; *sreekanth@iiap.res.in*

Received 2018 September 19; accepted 2018 December 15

Abstract We report atmospheric turbulence parameters, namely atmospheric seeing, tilt-anisoplanatic angle (θ_0) and coherence time (τ_0), measured under various sky conditions, at Vainu Bappu Observatory in Kavalur. Bursts of short exposure images of selected stars were recorded with a high-speed, frame-transfer CCD mounted on the Cassegrain focus of a newly commissioned 1.3 m telescope. The estimated median seeing is $\approx 1.85''$ at wavelength of ~ 600 nm, the image motion correlation between different pairs of stars is $\sim 44\%$ for $\theta_0 \approx 36''$ and mean τ_0 is ≈ 2.4 ms. This work was motivated by the design considerations and expected performance of an adaptive optics system that is currently being planned for the telescope.

Key words: atmospheric effects — turbulence — instrumentation: adaptive optics — catalogs — methods: observational

1 INTRODUCTION

The wavefront of a light beam arriving from distant astronomical sources is aberrated after passing through the turbulent layers of the Earth's atmosphere. Spatial and temporal inhomogeneities in the refractive index of air along the beam path produce random phase perturbations, impairing the performance of ground-based telescopes. The influence of wavefront distortion on an optical system was investigated by Fried (1965, 1966) using Kolmogorov's model of turbulence. The impact of spatial structure in atmospheric turbulence is described by Fried's parameter r_0, a standard measure of atmospheric seeing.

Normally, the image resolution varies depending on the seeing r_0, telescope aperture size D and exposure time t. For $D/r_0 > 1$ and central wavelength λ_0, the angular resolution of the telescope is limited to $\sim \lambda_0/r_0$, as opposed to the diffraction limited case of $\sim \lambda_0/D$. Furthermore, for seeing-limited observations the telescope sensitivity (number of photons received per unit area in the detector plane) scales with aperture as D^2, unlike the aberration-free case where sensitivity (Hardy 1998) is proportional to D^4.

The wavefront aberrations across the entrance pupil of a telescope are distributed over a large range of spatial frequencies. The lowest order aberration is the wavefront tilt which leads to overall angle-of-arrival fluctuations at the aperture plane. This time-varying tilt is responsible for short-exposure image motion (hereafter '*image motion*' means the motion of the centroid of a star image) at the detector plane. Fried (1975) derived the expression for the mean-square difference in angle-of-arrival of light as seen by two small sub-apertures separated by a certain distance that sample the wavefront of a single star, as shown in Figure 1. This forms the basis for most contemporary seeing measurements carried out with differential image motion monitors (Sarazin & Roddier 1990; Wilson et al. 1999; Tokovinin 2002).

Full potential of a ground-based telescope is realized by an adaptive optics (AO) system which measures the wavefront errors and applies corrections to compensate the tip-tilt, as well as the high-order aberrations which cause the blurring.

The wavefront sensing is done either on a bright science target or with a guide star – a naturally bright star or a laser beacon created in the close vicinity of a faint science target. The wavefront aberrations can differ significantly as the light from the guide star and science object take slightly different paths along the atmosphere. The decorrelation in wavefront errors along two propagation paths is a measure of anisoplanatism. The high order aberrations usually correlate well only over a small angular field ($\lesssim 10''$), while the correlation for lowest order tip-tilt typically extends beyond several 10s of arcseconds. The degree of correlation is again determined by the atmospheric seeing and angular

separation (McClure et al. 1991). The variance of wavefront tilt difference from two stars across a common telescope aperture, as illustrated in Figure 1, is generally referred to as *tilt-anisoplanatism*.

Previous attempts to measure tilt-anisoplanatism used binary stars at various angular separations. Those observations suffered from restricted bandwidth limitations and lack of bright star pairs at specific angular separations. An early measurement of tilt-anisoplanatism was reported by Teoste et al. (1988) with the 1.2 m Firepond facility, administered by Lincoln Laboratory. In that experiment, two quad trackers measured the differential tilt between three binary star pairs with separation varying from $10''$ to $22''$.

Subsequently, Sivaramakrishnan et al. (1995) used a fast readout CCD to capture multiple stars inside a single frame. A linear rise in standard deviation of differential tilt was observed for star separation varying from $10''-58''$. In another experiment, images of the Moon's edge were used to obtain a statistical estimate of tilt angular correlation and tilt averaging functions over a continuous wide range of angular separations (Belen'kii et al. 1997).

The turbulence also produces temporal phase fluctuations along with spatial distortions in wavefront. These fluctuations are characterized by atmospheric coherence time (τ_0). Within this time limit, the phase fluctuations are negligible. In AO systems, time interval between wavefront sensing and correction should be constrained within unit τ_0. Thus, it requires a temporal closed loop bandwidth $\gg 1/2\pi\tau_0$.

As τ_0 is dependent on r_0 and wind velocity, its measurement using short exposure images is influenced by data sampling time (Hardy 1998). Because of this, different definitions of coherence time for phase fluctuations given by Breckinridge (1994) differ by a factor as large as 7. Based on these approximations, Davis & Tango (1996) explained the effect of data sampling time on the measurement of turbulence. These earlier analyses mentioned the optimum sampling time on the order of a few milliseconds.

These experiments emphasize the usefulness of fast, short exposure images of a star in determining crucial atmospheric turbulence parameters such as seeing (λ/r_0) and atmospheric time constant (τ_0), and several pairs of stars can be used to measure tilt-anisoplanatic angle (θ_0) (Martin 1987; Davis & Tango 1996; Kellerer & Tokovinin 2007).

We used short exposure images for estimation of the atmospheric turbulence parameters, obtained with the 1.3 m telescope at Vainu Bappu Observatory in Kavalur. Short exposure images of selected stars were taken with a high-speed CCD camera.

We exploited the ability to define multiple regions of interest (ROIs) within the CCD frame to record simultaneous position measurements of stellar images with large angular separation up to $\approx 212''$, at the image plane for measurement of θ_0.

The rest of this paper is organized as follows. The details of the high speed imaging camera, target selection criteria, observation methodology and data analysis are provided in Section 2. In Section 3, we describe the seeing measured from the root mean square (rms) image motion and compare it with that measured from other methods. In Section 4, we explain the measurement of tilt-anisoplanatic angle. In Section 5, we describe the estimation of the atmospheric coherence time τ_0. In Section 6, we discuss relevance of these parameters in designing an AO system for the telescope. Finally, in Section 7, we summarize the results.

2 TARGET SELECTION AND OBSERVATIONAL METHODOLOGY

The 1.3 m telescope at Vainu Bappu Observatory, Kavalur, was commissioned in the year 2014. It is a Ritchey-Chrétien telescope with hyperbolic primary and secondary mirrors. The telescope is located at an elevation of 750 m above mean sea level in the Javadi Hills in southern India at $78^\circ 50'$E and $12^\circ 34'$N. Because the telescope has user friendly operation, and has better tracking and better optical quality, it was chosen for technology demonstration of an AO system. Prior to the development of an AO system, on-site estimation of turbulence parameters could provide crucial information for the design of such a system. Thus, a study of turbulence parameters started on-site for the 1.3 m telescope during the 1st quarter of 2016. The relevant specifications of the telescope are given in Table 1.

2.1 High Speed CCD Camera

Rapid imaging requires a high speed CCD. It is desired to have continuous exposure with minimum time lag between two successive frames. For tilt isoplanatic angle measurements, two or more objects need to be observed simultaneously in a given field. The lower and upper limits of angular separation between two objects is set by the resolvability between the two objects and the CCD size, respectively. The large separation between the objects occupies larger frame size and thus requires more readout time. To avoid reading unnecessary pixels, new technology also permits the selection of multiple ROIs on the CCD. This useful functionality can further reduce the readout time.

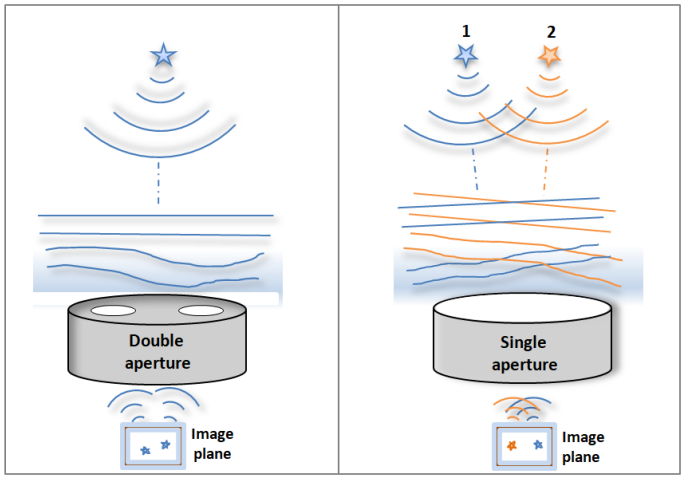

Fig. 1 Illustration of measuring differential tilt of a stellar wavefront sampled at different locations by two sub-apertures (*left panel*) and differential tilt between a pair of stars within the field of a mono-pupil telescope (*right panel*).

Table 1 Specifications of J. C. Bhattacharya Telescope and CCD

Property	Value
Primary aperture diameter	1.3 m
Focal length	10.4 m
F ratio	8
Central obscuration	42 cm
Mount type	Equatorial
Camera	Princeton Instruments ProEM xEcelon[1]
Detector size	1024×1024
Pixel size	13 μm
Pixel scale	$0.26''$
FoV	$\approx 4' \times 4'$
Gain	1.37 e^- ADU^{-1}
Read Noise	10.35 e^-
Bit depth	16 bit $pixel^{-1}$
Read out type	Frame transfer
Read out rate	10 MHz

[1] *https://www.princetoninstruments.com/userfiles/files/assetLibrary/Datasheets/ProEM-HS-1024BX3-and-1KBX3-10um-datasheet-P4-5-16-17.pdf.*

We used Princeton Instruments ProEm eXcelon (1024×1024, pixel size = 13 μm) EMCCD[1] for our observations. The CCD used frame transfer mode for continuous exposure and simultaneous readout. In this mode, the detector has active and masked areas. After the exposure, the data are vertically (parallel) shifted from active area to masked area. This shift occurs within a few microseconds. Thus, the active area is immediately available for the next exposure[2] while the image is read out from the masked section. The time lag between two successive frames is 0.8 μs. The current version of the CCD can read out the data with 10 MHz clock speed. It has quantum efficiency (QE) $\approx 90\%$ for the visible wavelength band[3]. The full frame of the CCD covers $\approx 4' \times 4'$ on-sky field of view (FoV) with plate scale of $0.26''$ $pixel^{-1}$. The CCD has an option to capture multiple ROIs within a single frame with user defined window size for each. The CCD specifications are given in Table 1.

2.2 Observation Methodology

The telescope is used for intensive observations in rapid imaging mode. For the operation, target selection with respect to their magnitude, hour angle and declination is crucial. These variables influence the estimation of turbulence parameters.

A list of targets was chosen that satisfy the following criteria. The targets should be bright enough to have sufficient signal to noise ratio (SNR), and the pair should be spatially resolved and fall within the CCD frame. Thus, multiple pairs of stars with magnitude up to $m_v \approx 8$ and on-sky angular separation ranging from $6.4'' - 212''$

[1] *https://www.princetoninstruments.com/userfiles/files/*

[2] ProEM EMCCD Camera Systems, *ftp://ftp.piacton.com/Public/Manuals/Princeton*

[3] Princeton Instruments ProEMCCD, *https://www.princetoninstruments.com/userfiles/files/assetLibrary/ Datasheets/ProEM-HS-1024BX3-and-1KBX3-10um-datasheet -P4-5-16-17.pdf*

Table 2 List of observed stars with varying angular separations. In this table, 'Dec' is declination of the object, 'RA' is right ascension, 'm_v' is apparent magnitude, 'Δm_v' is magnitude difference between two objects and 'Sep' is angular separation between the objects in arcseconds.

Object	Dec	RA	m_v	Δm_v	Sep ($''$)
HR4414	02 55 39	11 26 45.3	6.5	1.1	28.5
HR3174	–09 17 25	08 06 27.4	6.23	1.7	30.8
HR3428	19 37 50	08 40 20.7	6.44	1.3	63.2
HR4752	25 49 26	12 28 54.7	5.29	1.4	145.4
HR4884	17 00 33	12 52 12.2	6.32	0.6	196.5
HR5010	19 48 03	13 16 32.1	6.49	1.9	203
HR4085	02 18 10	10 24 13.0	6.32	0.3	212
HR4128	–15 15 43	10 47 37.9	6.67	1.2	74.7
HR4193	04 44 52	10 43 20.9	5.79	1.1	6.7
HR4259	24 44 59	10 55 36.7	4.5	1.9	6.5
HR4677	–03 57 14	12 18 09.2	6.99	0.4	20.1
HR7593	–08 13 38	19 54 37.7	5.71	0.8	35.7
HR7672	17 04 12	19 51 17.7	5.8	0.9	203.7
HR7705	20 53 48	20 09 56.6	6.48	0.6	83.9
HR7830	–18 35 00	20 29 53.9	5.94	0.8	21.9
HR7840	11 15 39	20 31 13.1	7.11	0.3	16.7
HR8265	06 37 06	21 37 43.6	6.18	1.5	39.5
HR8619	–28 19 32	22 39 44.2	6.31	1.3	86.6
HR9002	–18 40 41	23 46 00.9	5.29	1	6.6
HR9044	–27 02 32	23 54 21.4	6.35	0.7	6.4
HR310	21 28 24	01 05 41.0	5.34	0.3	29.9
HR313	01 92 24	01 05 49.1	6.35	1	33
HR545	19 17 45	01 53 31.8	4.83	0.1	7.8
HR765	24 38 51	02 37 00.5	6.5	0.6	38.3
HR1065	27 34 19	03 31 20.8	5.96	0.4	11.4
HR1212	–01 12 15	03 54 17.5	4.79	1.5	6.8
HR1322	02 51 62	04 15 28.8	6.31	0.6	64.7
HR1460	–09 44 12	04 35 14.1	6.37	1	12.8
HR1505	–08 47 38	04 43 34.7	6.82	0.1	9.3
HR1600	14 32 34	04 58 59.4	6.09	1.5	39.3
HR1610	03 36 58	05 00 33.9	6.66	0.4	21.3
HR1619	01 36 32	05 02 00.0	6.24	1.3	14.2
HR1753	–18 31 12	05 19 17.4	6.36	0.2	39.3
HR2174	02 29 58	06 08 57.8	5.73	1.2	29.3
HR2356	–07 01 59	06 28 48.9	4.6	0.5	7.1
HR2948	–26 48 07	07 38 49.3	4.5	0.2	9.9
HR3010	–14 41 27	07 45 29	6.07	0.8	16.8
HR3028	–16 00 52	07 47 45.2	6.43	0.1	130.5

were chosen. The target objects are referenced from the Catalogue of Bright Stars (Hoffleit 1964). The list of observed objects (brighter companion in each pair) is compiled in Table 2.

The observations made on selected targets were carried out from evening to midnight. The reason for restriction post midnight is the unprecedented rise in relative humidity (RH), to greater than 90%. High RH could cause irretrievable damage to the optics and electronic systems of the telescope. Thus, the observations were confined to below 85% RH.

The short exposure images of individual stars within the CCD FoV were acquired using the ROI technique as illustrated in Figure 5. The ROI size varied from 30×30 pixels to 45×45 pixels. This varying size is chosen to confine the image motion within the specified ROI window. This of course depends upon the prevailing seeing conditions and duration of each observation run. The exposure time is 8–25 ms and each target pair is observed for 10 000–100 000 frames over $\approx 4-25$ minutes.

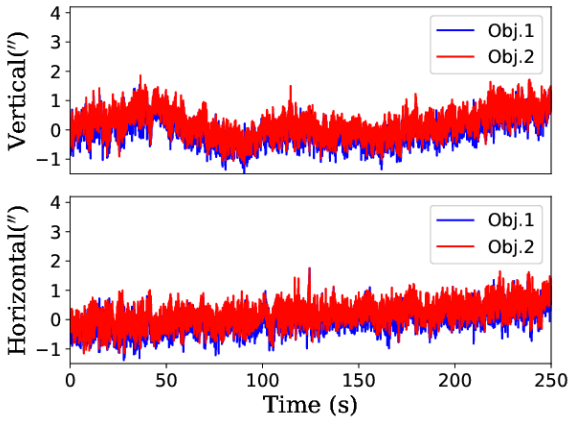

Fig. 2 Absolute motion of image centroid along the horizontal axis (H) and vertical axis (V) of the CCD for object 1 (HR4414) and object 2 (83 Leo B) of the target pair. In this image, the X-axis is duration of the observation in seconds and Y-axis is centroid motion of the objects in arcseconds ($''$).

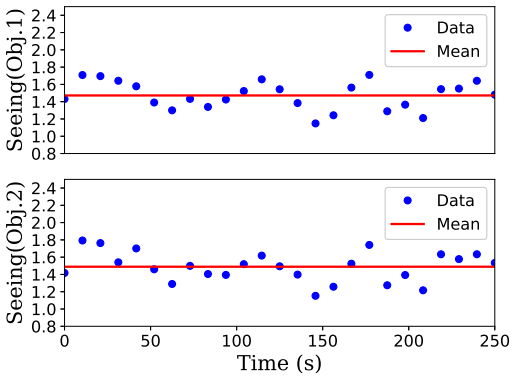

Fig. 3 Atmospheric seeing measured from the rms data of the centroids of object 1 (*top*) and object 2 (*bottom*). Seeing ($''$) is measured every 10 seconds. The *bold lines* are the mean seeing. The measured mean seeing is $\approx 1.49'' \pm 11\%$ for both objects.

All our observations are confined to R-band with a peak at $\approx$ 600 nm. The details about the observations are summarized in Table 3.

2.3 Data Analysis

Raw data from the CCD are in *.spe* format. This is a binary data format with distinct sections of header, data and footer. The header contains offset locations of data, time and duration of observation, ROI position on CCD frame,

Fig. 4 The aperture geometry used in simulating the theoretical transfer functions and estimating the spectral ratio constants. The *black regions* indicate central obscuration and spiders holding the secondary. The *white region* signifies the useful aperture area.

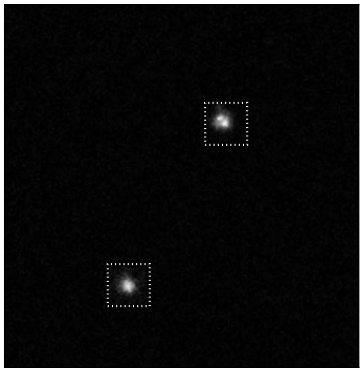

Fig. 5 A sample frame with two target stars observed on 2015 April 6. The object in the top-right (HR4414) has an apparent magnitude $m_v = 6.5$ and that on the bottom-left (83 Leo B) has $m_v = 7.6$. The angular separation between the two stars is $28.5''$. The *dotted squares* indicate the ROI window around each target.

ROI window size, target of observation, etc. Each observation of a target is placed in a single binary data file. Prior to data processing, all the image frames need to be unstacked.

A code is developed in Python software to unstack each of the image frames. As initial step, it could read the number of frames, the offset position, dimensions and number of ROIs. The unstacked frames are available for data processing.

Each of the data frames is cleaned prior to analysis. For this, early sky flats have been captured once in a month to know the QE of the CCD pixels, known as flat frames. From the available flat frames we used median count to construct the master flat frame. Dark frames were taken for each observation of the target. A master dark frame was created by finding the median of dark frames. To minimize the effect of noise, the master dark was subtracted from each data frame and divided by the master flat frame. Thus the resultant data were cleaned from bias and flat field errors.

Table 3 Observation Details

Parameter	Value
Wavelength	R-band filter (peak at 600 nm)
ROI size	30×30 to 45×45 pixels
Exposure time	8–25 ms
Magnitude	$m_v < 8$
Hour angle	± 1 h
Declination	$\pm 30^\circ$
Air mass	≤ 1.34
Duration per target	$\approx 4 - 25$ min
Frames per target	10 000–100 000
Number of nights	29
Total number of observations	248

2.4 Centroid Estimation

Image motion is estimated by using its centroid. The centroid region is limited to a window of 10×10 pixels surrounding the maximum intensity pixel and intensity thresholding is applied. This exercise aims to minimize the effect of noise. The first order intensity weighted method is used to estimate the centroid of the clean data.

$$X_c = \frac{\sum x_i I_i}{\sum I_i} , \qquad Y_c = \frac{\sum y_i I_i}{\sum I_i} , \tag{1}$$

$$\sigma_x = \sqrt{\frac{\sum (X_c - \bar{X_c})^2}{n}} , \qquad \sigma_y = \sqrt{\frac{\sum (Y_c - \bar{Y_c})^2}{n}} , \tag{2}$$

where X_c, Y_c the estimate centroid coordinates of an image, $I_{i,j}$ are pixel intensities, $x_{i,j}$, $y_{i,j}$ are coordinates of pixels, $\bar{X_c}$, $\bar{Y_c}$ are the mean value of centroids and σ_x, σ_y are the rms error in centroids.

In Figure 2, the centroid motion of star 1 (HR4414) and star 2 (83 Leo B) along horizontal axis (H) and vertical axis (V) of the CCD is plotted. Both objects were observed simultaneously.

3 ESTIMATION OF SEEING

Fried's parameter r_0 is a single parameter used to represent the turbulence strength (Fried 1966). It is defined as the spatial scale at which the rms phase variation is one radian in the distorted wavefront. It is dependent on the refractive index structure constant of a turbulent medium, wavelength and zenith angle of the observations. Refractive index structure constant is integrated over multiple layers of the atmosphere and it varies randomly with time. This generates continuous random fluctuations in r_0. Instantaneous variations of this parameter cause random motion and blurring of the image. In practice, the image quality is expressed as λ/r_0, also known as *seeing*.

3.1 Seeing Using rms Image Motion

We estimated the *seeing* from the motion exhibited by a burst of short exposure images. Essentially, r_0 was estimated from the images using Equation (3) (Martin 1987).

$$\frac{r_0}{1\mathrm{m}} = \left[\frac{0.0431}{\sigma}\frac{\lambda}{0.5\mu}\left(\frac{d}{1\mathrm{m}}\right)^{-\frac{1}{6}}\right]^{\frac{6}{5}} . \qquad (3)$$

Here, σ is the rms of the image motion, estimated over a 10 s interval of data. As a result, this expression gives r_0 for every 10 s and mean r_0 is calculated for the entire duration of each observation. The estimated r_0 (cm) is converted to atmospheric seeing ($''$). In Figure 3, the estimated seeing for object HR4414 is plotted. The mean seeing measured from this observation is $1.49'' \pm 11\%$.

3.2 Seeing Using FWHM

The mean seeing measured from the aforesaid method is compared with the full width at half maximum (FWHM) of the long exposure image. In this case, the long exposure image is obtained by co-adding the short exposure images as they have negligible time interval between them. The FWHM of a long exposure image is a standard estimation of atmospheric seeing conditions. Assuming negligible tracking errors within a time span of 10 s, one can estimate FWHM every 10 seconds and hence the mean seeing for a full length of the observation. The FWHM is related to r_0 as $0.98\lambda/r_0$ and r_0 (cm) is converted to seeing ($''$). The measured seeing for the object HR4414 is $1.54'' \pm 9\%$.

3.3 Seeing Using Spectral-ratio Method

Estimation of r_0 using the spectral ratio method was formulated by von der Luehe (1984). In this method, the squared modulus of ensemble averaged Fourier transform of an image ($S_i(\bar{q})$) is divided by the ensemble averaged power spectrum of that image. The observed radial profile is compared with the theoretical model to estimate r_0. The expression for the spectral ratio method reads as follows

$$\varepsilon(\bar{q}) = \frac{|\langle S_i(\bar{q})\rangle|^2}{\langle |S_i(\bar{q})|^2\rangle} , \qquad (4)$$

$$E[\varepsilon(\bar{q})] = \frac{E[|\langle S_i(\bar{q})\rangle_{SE}|^2]}{E[\langle |S_i(\bar{q})|^2\rangle]} . \qquad (5)$$

In Equation (5), $E[...]$ denotes an ensemble average.

The radial profiles obtained from observational data and theoretical model have been overplotted to estimate seeing. The model is simplified and it is expressed in terms of q and α, where q is wavenumber and α is modified Fried's parameter. The wavenumber is defined as the ratio of spatial frequency and theoretical cut off frequency of the telescope $f_c = \frac{D}{\lambda R}$, whereas D is diameter, R is focal length of the telescope and λ is light wavelength. The modified Fried's parameter α is given as r_0/D.

$$\alpha = Aq^B \; \forall \; \alpha \leq 0.3 . \qquad (6)$$

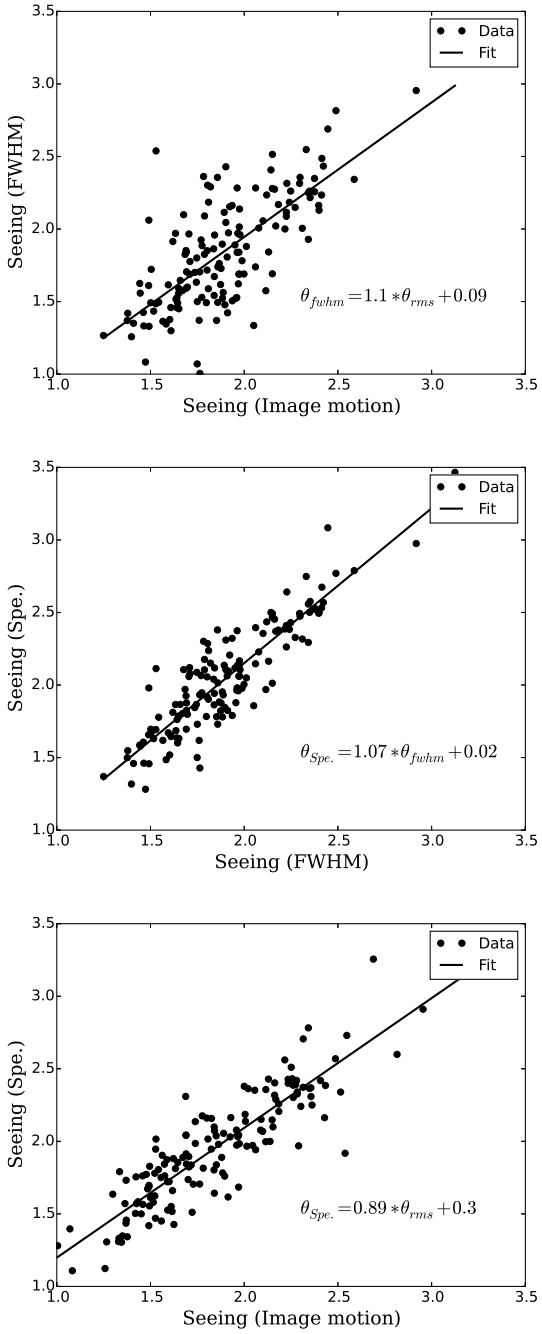

Fig. 6 Seeing measured from centroid motion of object (rms), FWHM and spectral ratio (Spe.) method has been compared. The units of the axis are in arcseconds. The data points in this plot are seeing measured for the targeted objects. The *solid line* is the approximate relation between seeing measured from both methods. A linear model has been fit to the data obtained and the relation between them is shown in the plot.

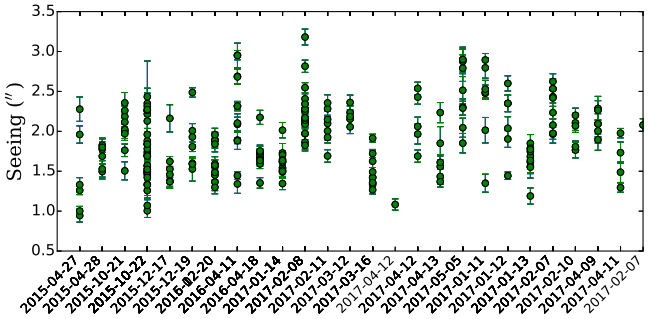

Fig. 7 Each of the data points with error is mean seeing ($''$) estimated for each observation. The plot is the result of 248 observations of more than 50 targets observed in 29 nights over a period of 2 years. On average, the error in each estimation is $\approx \pm 11\%$. The vertical projection of data points is the mean seeing of the observations during the same night. The projection is as high as $1.5''$.

The coefficients A and B have been chosen such that the falling end of the radial profiles for the observational and theoretical models will coincide. The r_0 of observational data is obtained by finding the better represented theoretical radial profiles (von der Luehe 1984).

We estimated r_0 using this method after incorporating the following two changes: First, we estimated the library of short exposure transfer functions and the speckle transfer functions numerically for our annular aperture geometry (c.f. Fig. 4) assuming a Kolmogorov turbulence model atmosphere. We then estimated the spectral ratio constants A and B using the numerically simulated spectral ratio.

After estimating the theoretical spectral ratio constants for our annular aperture, we used them to estimate r_0 for our observed data. For the object HR4414, the mean was found to be $1.71'' \pm 13\%$.

3.4 Comparison of r_0

The seeing estimated using the image motion method, the FHWM and the spectral ratio method has been compared and the results obtained from these methods are presented in Figure 6. It is found that the seeing estimated from the aforesaid methods has correlation of $\approx 86\%$ (mean of the three correlations). Our observation is that the r_0 estimated from the angle of arrival fluctuation method is higher than that from the spectral ratio method and it is consistent with what has been reported in the literature elsewhere (Goode et al. 2000). However, the exact ratio in our case is 1.14 and it is less than that reported by Goode et al. (2000). Given that there is good correlation between the values estimated from different methods, hereafter we refer to the value estimated from the rms image motion in our discussions.

3.5 Long Term Measurement of r_0

In Figure 7, seeing estimated from rms image motion is plotted against the civil day of observation. It contains mean seeing from 248 observations on more than 50 targets (including the list shown in Table 2) observed over 2 years. The vertical line along any night shows the temporal variation of the seeing over the time period of observations. This happens because the atmospheric turbulence causes temporal fluctuations in r_0. This varies with time, position of the target and depends on several observational conditions. The mean seeing of the telescope site is evaluated as the statistical average of the estimated seeing over the entire duration of observations. It is estimated as $1.89'' \pm 11\%$. The probability density of observed seeing is plotted in Figure 8. A normalized distribution of the data is plotted over the histogram. The median seeing at the telescope site is observed as $\approx 1.85''$.

4 ESTIMATION OF TILT-ANISOPLANATIC ANGLE

To estimate θ_0, several pairs of stars separated by an angle θ, at the image plane, have been considered. Table 2 indicates the targets selected for the estimation. Each of the star pairs with ROIs is observed simultaneously with an exposure time of 25 ms. The limitation on exposure time is due to minimum time required to read out a CCD frame (2 ROIs with 40×40 pixels). The duration of observations for each target is ≈ 4 minutes, and it corresponds to about 10 000 frames. To quantify the relation in their image motion, the centroids of the images are correlated. An expression that is used for the measurement of correlation coefficient (ρ) is shown in Equation (7). This parameter is measured for several pairs of stars with different angular separations.

$$\rho_x = \frac{\sigma_{x1x2}}{\sqrt{\sigma_{x1}\sigma_{x2}}}, \quad \rho_y = \frac{\sigma_{y1y2}}{\sqrt{\sigma_{y1}\sigma_{y2}}} \, . \tag{7}$$

In the above equation, σ_{x1x2}, σ_{y1y2} are the covariance of the image centroid motions for object 1 and object 2 along the H and V axes respectively, σ_{x1}, σ_{x2}, σ_{y1}, σ_{y2}

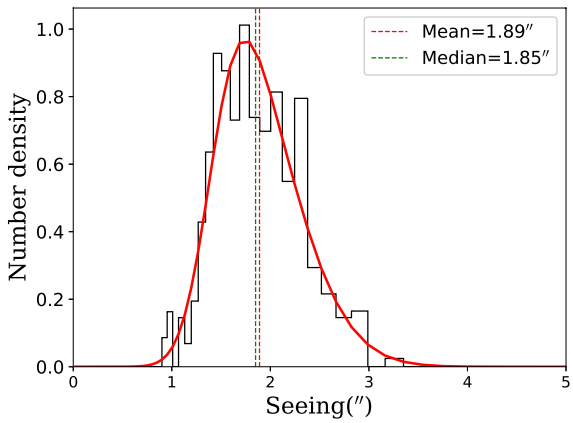

Fig. 8 Probability density of seeing values and log-normal distribution. The mean and median seeing observed from the data are $1.89'' \pm 11\%$ and $1.85''$ respectively.

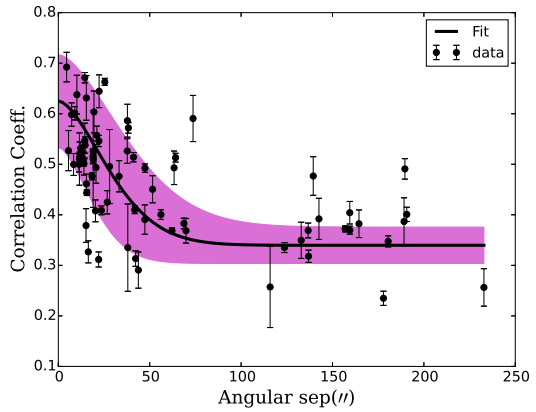

Fig. 9 The relation for the image motion correlation between stars of a target with respect to the angular separation between them. The plot has 73 observational data points. The X-axis and Y-axis are the angular separation in arcseconds ($''$) and correlation coefficient respectively. The data have an estimated error as high as $\approx 21\%$. Approximately, 60% and above of correlation is present at an angular separation of $12''$. The thick band in orchid color is the 5σ level of error estimation. The empirical relation between ρ and θ is mentioned.

are image motion variance (same as Equation (2)) of objects 1 and 2, and ρ_x, ρ_y are correlation coefficients of the image centroid motion along the two orthogonal axes. The estimated ρ is the mean of ρ_x and ρ_y.

The observational data are shown in Figure 9 where ρ is plotted against θ. It is evident that ρ is inversely related to θ. Even though image motion correlation is largely dependent on θ, it is also influenced by seeing and wind speed during the observation and zenith angle of the target. The effects of these parameters on the measurement of ρ occur in the image centroid motion. Thus the measured value of ρ is not purely due to θ, but rather it is the integrated effect of all these parameters.

$$\rho = a_1 + a_2 \exp[-(\theta/\theta_0)^{5/3}] \, . \tag{8}$$

θ_0 is obtained from an empirical relation derived from the statistical relation between ρ and θ. To obtain such relation, an analytical expression (Eq. (8)), based on the Kolmogorov turbulence model, has been fit to the observational data. In Equation (8), ρ is correlation coefficient, a_1, a_2 are coefficients and θ, θ_0 are angular separation and isoplanatic angle respectively. A least squares approximation model is fit to the data to estimate these parameters. From this approximation, it is estimated that $a_1 \approx 0.34$, $a_2 \approx 0.29$ and $\theta_0 \approx 36''$.

The fitted data plot is drawn in a solid line in the Figure 9. The thick band in orchid color shows the 5σ level of error estimation. Most of the data fall within this limit. The figure shows that the image motion correlation between two objects has a declining trend with increase in angular separation. Approximately, 60% of the correlation has been observed down to an angular separation of $12''$. The correlation coefficient has reached $\approx 44\%$ at a separation of $\approx 36''$. This model equation is valid for objects with angular separation $(\theta) \gtrsim 6.4''$, as is the case with our data set.

5 ESTIMATION OF COHERENCE TIME

We adopted the following procedure to estimate the atmospheric coherence time (τ_0) from the series of short exposure images. The general idea is to extract a series of phase fronts from the series of short exposure images. We make use of the Fourier transform relationship between the image plane and the telescope pupil plane, and apply the Gerchberg-Saxton algorithm (Gerchberg 1972) to recover, iteratively, the complex phase distribution in the pupil plane. We then extract the phase from this complex distribution using a phase-unwrapping algorithm[4]. The iterative procedure is illustrated in Figure 10.

The rms phase variations of the pupil plane phase ϕ corresponding to each frame are estimated. We define temporal phase structure function D_ϕ as given in Equation (9) and model the same as in Equation (10).

$$D_\phi(\tau) = \langle |\phi(t) - \phi(t+\tau)|^2 \rangle \, , \tag{9}$$

$$D_\phi(\tau) = \left(\frac{\tau}{\tau_0}\right)^\beta \, , \tag{10}$$

where the angular brackets indicate ensemble average, τ is time to acquire an image, τ_0 is the coherence time and β is a constant.

[4] Phase Unwrapping, `https://scikit-image.org/`

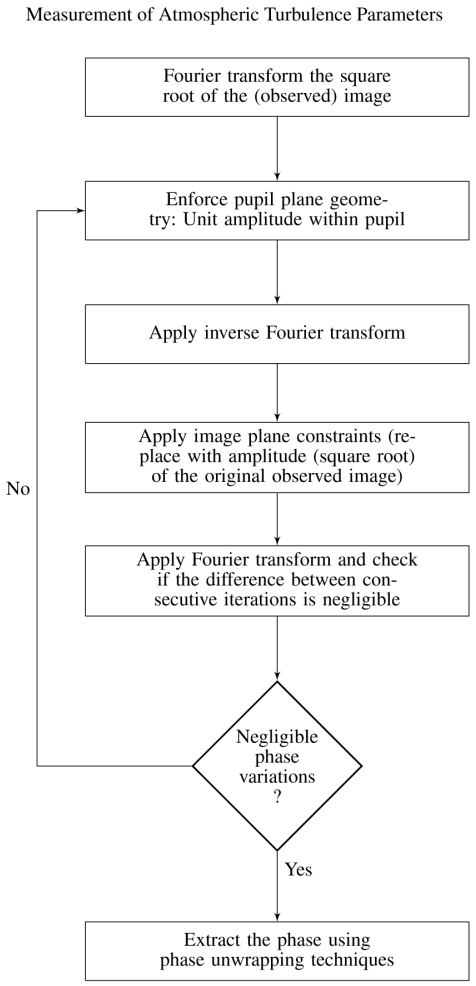

Fig. 10 Flow chart to extract phase fronts from observed images.

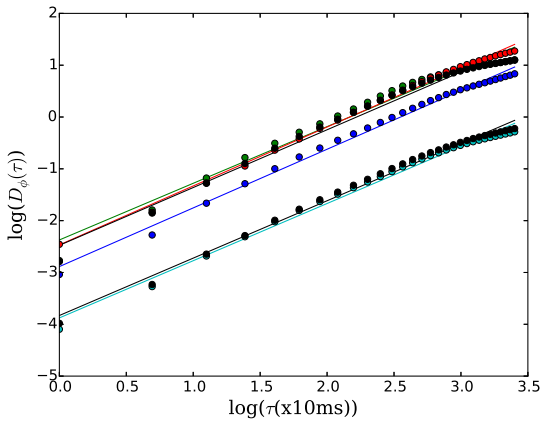

Fig. 11 Log amplitude of temporal phase structure function. It is an ensemble average of the rms phase variations of star images with time. The X-axis is time and the Y-axis is log amplitude of the structure function. The data points in the plot are obtained from the observational data and the solid lines are the model fit to the structure function.

Table 4 Turbulence coherence time estimation. It is measured for different targets during the same night. The presented data are from the observation conducted on 2015 April 27. The data contain the power value of the structure function and the coherence time. The mean coherence time is ∼2.4 ms.

Object	β	τ_0 (ms)
HR4128	1.13	1.49
HR4414	1.10	3.54
HR4752	1.14	2.53
HR4884	1.12	2.47
HR4085	1.10	2.42
HR5010	1.02	1.90

To simplify the model fitting, Equation (10) is rewritten in logarithmic scale. The resultant linear equation is given below.

$$\log[D_\phi(\tau)] = \beta[\log(\tau) - \log(\tau_0)] \; . \qquad (11)$$

Both β and τ_0 are estimated from the model.

The theoretical value of β is $5/3$ for Kolmogorov turbulence. β and τ_0 are estimated for a few representative cases, by fitting the model to the estimated structure functions (Fig. 11).

The estimated values of τ_0 and β for a few representative cases are provided in Table 4. It indicates that the coherence time varies between 1.5 ms and 3.5 ms, and β varies between 1 and 1.4.

6 DISCUSSION

We have estimated a median atmospheric seeing of $\approx 1.85''$, tilt-anisoplanatic angle of $\approx 36''$ for 44% image motion correlation and a mean coherence time of ≈ 2.4 ms.

In what follows, we shall now discuss how these values play a decisive role in designing an AO system for our 1.3 m telescope at Vainu Bappu Observatory. We will discuss how knowledge of these parameters helps to specify the stroke needed for the deformable mirror, the temporal frequency required for the data acquisition and the effectiveness of AO correction from the lock position.

We will arrive at the stroke required, assuming that the AO system should be operable when r_0 is as low as 5.5 cm. The residual rms wavefront error at 600 nm in the instantaneous wavefront (i.e. excluding the tip and tilt) is shown in Equation (12) (Tyson 1998).

$$\sigma = 0.366 \frac{\lambda}{2\pi} \left(\frac{D}{r_0} \right)^{5/6} = 0.512 \; \mu\text{m} \; . \qquad (12)$$

Assuming a 5σ level for the instantaneous wavefront, the peak wavefront error is 2.56 µm. It should be noted that with the reflective geometry, the actual stroke needed will be half of this value. Thus, a deformable mirror with maximum stroke of ∼3 µm should be a conservative up-

per limit. If we specify a 0.1 Strehl ratio at 600 nm, the residual mean square wavefront phase error is 2.3 radian^2. Assigning 1/3 weight to the wavefront fitting error, we arrive at the number of actuators N using the expression given by Hardy (1998).

$$\sigma_{\rm fitting} = 0.3N^{-5/6}(D/r_0)^{5/3} \ . \qquad (13)$$

By substituting the values, we get $N \sim$183. Thus, we would require about 180–200 actuators in our system.

The wavefront correction needs to be applied within one coherence time τ_0. The closed loop correction bandwidth is $\sim \frac{1}{2\pi\tau_b}$ where τ_b is the time gap between the wavefront sensing and the wavefront correction. Assuming a factor of six to ten times the closed loop correction bandwidth is required for the AO loop, we arrive at the loop frequency of $\sim$400–600 frames per second.

Tilt-anisoplanatic angle (θ_0) is an important parameter for natural guide star AO systems. As discussed in the Introduction, the better choice of reference object is its proximity to the target, so that the AO system performance will be effective. Thus it limits the effectively corrected FOV for observations. In our case, when we use a bright reference object nearby our target of interest, their angular separation should be less that $36''$ so that at least the tilt component of the wavefront correction will be effective.

7 SUMMARY AND CONCLUSIONS

(1) We have estimated r_0 (or alternatively the seeing) from 248 distinct observations spanning over 29 days, making use of fast CCD images and measured r_0 from angle of arrival fluctuations. We compared the estimated values with those estimated from other methods and found that the values match with 14% uncertainty.

(2) With the limited data, the median seeing at 600 nm is found to be $1.85''$, the tilt-anisoplanatic angle θ_0 is $36''$ for 44% correlation and the atmospheric coherence time, estimated for six different observations, is $\sim$2.4 ms.

(3) The estimated parameters should be considered as preliminary, because the values are likely to change with further data. Nevertheless, they help in identifying the design parameters of the AO system to be built on this telescope.

(4) The observed values reinforce the need to construct an AO system for achieving diffraction limited resolution. An infrared AO system will be preferable as the coherence time is likely to be better than what has been observed in the near-infrared R band.

Acknowledgements We would like to thank Mr. P. Anbhazagan, field officer in-charge of Vainu Bappu Observatory in Kavalur for his valuable support and observing assistants V. Moorthy, G. Selvakumar and S. Venkatesh for their help during the course of this work.

References

Belen'kii, M. S., Karis, S. J., Brown, II, J. M., & Fugate, R. Q. 1997, in Proc. SPIE, 3126, Adaptive Optics and Applications, eds. R. K. Tyson, & R. Q. Fugate, 481

Breckinridge, J. B., ed. 1994, Proc. SPIE, 2200, Amplitude and Intensity Spatial Interferometry II

Davis, J., & Tango, W. 1996, PASP, 108, 456

Fried, D. L. 1965, Journal of the Optical Society of America (1917–1983), 55, 1427

Fried, D. L. 1966, Journal of the Optical Society of America (1917–1983), 56, 1372

Fried, D. L. 1975, Radio Science, 10, 71

Gerchberg, R. W. 1972, Optik, 35, 237

Goode, P. R., Wang, H., Marquette, W. H., & Denker, C. 2000, Sol. Phys., 195, 421

Hardy, J. W. 1998, Adaptive Optics for Astronomical Telescopes (Oxford Univ. Pres), 448

Hoffleit, D. 1964, Catalogue of Bright Stars (3rd edn.; New Haven, Conn.: Yale Univ. Observatory)

Kellerer, A., & Tokovinin, A. 2007, A&A, 461, 775

Martin, H. M. 1987, PASP, 99, 1360

McClure, R. D., Arnaud, J., Fletcher, J. M., Nieto, J.-L., & Racine, R. 1991, PASP, 103, 570

Sarazin, M., & Roddier, F. 1990, A&A, 227, 294

Sivaramakrishnan, A., Weymann, R. J., & Beletic, J. W. 1995, AJ, 110, 430

Teoste, R., Daley, Jr., J. A., Capes, Jr., R. N., Alves, J. J., & Zimmerman, M. D. 1988, Measurements of Tilt Anisoplanatism at the Firepond Facility, Tech. Rep. (Massachusetts Inst Of Tech Lexington Lincoln Lab)

Tokovinin, A. 2002, PASP, 114, 1156

Tyson, R. K. 1998, Principles of Adaptive Optics (Principles of Adaptive Optics, (2nd edn.; Boston: Academic Press)

von der Luehe, O. 1984, Journal of the Optical Society of America A, 1, 510

Wilson, R. W., O'Mahony, N., Packham, C., & Azzaro, M. 1999, MNRAS, 309, 379